J Therm Anal Calorim (2016) 125:1009–1015
DOI 10.1007/s10973-016-5482-y

Melting behavior and oxidation resistance of Ce–Sn alloy designed for lead-free solder manufacturing

Marian Drienovsky[1] · Lydia Rizekova Trnkova[1] · Milan Ozvold[1] · Ivona Cernickova[1] · Marian Palcut[1] · Jozef Janovec[1]

Received: 2 October 2015 / Accepted: 12 April 2016 / Published online: 29 April 2016

Abstract Ce–Sn pre-alloy (master alloy) was designed for new lead-free solder alloy manufacturing. The microstructure characterization revealed the presence of $CeSn_3$ particles in the Sn matrix. The melting behavior in air was investigated by differential thermal analysis coupled with thermogravimetric analysis. When melting was finished, the pre-alloy started to oxidize instantly, because of a high affinity between $CeSn_3$ and Ce itself to oxygen. The oxidation process of Ce–Sn pre-alloy is described in detail. The solidus (231 °C) and liquidus (485 °C) temperatures of the alloy were determined by differential scanning calorimetry (DSC). By repetitive DSC measurement, it has been verified that this alloy had to be re-melted in an inert gas atmosphere to prevent oxidation. The master alloy is ultimately used to produce new Ce-containing Sn–Ag–Cu solder alloys.

Keywords Ce–Sn alloy · DTA–TG–DTG · Oxidation · Lead-free solder

Introduction

Rare earth (RE) elements, such as Ce, La or Nd, are known as "vitamins of metals". Many researches [1–5] introduce them into aluminum or magnesium alloys in order to modify their microstructure and improve their mechanical properties. RE elements have also found their way into lead-free solder alloys composed of Sn, Ag, Cu and Bi in respective eutectic [6–8], near-eutectic [9, 10] or non-eutectic concentrations [11, 12]. The presence of RE in lead-free solder alloys in small amounts has been found to improve a number of their properties [13–16]. For instance, we investigated earlier the effect of Ce concentration on microstructure refinement, melting behavior and mechanical properties of a series of near-eutectic Sn–Ag–Cu alloys [13, 14]. It was found that Ce addition up to 0.1 mass% can refine the microstructure, reduce the undercooling effect during alloys solidification and enhance the mechanical strength of the alloy. However, if this concentration threshold is exceeded, small $CeSn_3$ particles in the alloy microstructure are formed and mechanical properties are significantly deteriorated.

Since RE elements have a high affinity toward oxygen [17], the preparation of solders by direct melting of Sn, Ag, Cu and Ce can be quite demanding. Hence, binary pre-alloys (Ce–Sn or Ce–Cu) are usually designed to make the Sn–Ag–Cu–Ce solder alloys manufacturing process easier [18–22]. Although the thermodynamic properties of Ce–Sn and Ce–Cu binary systems are well described in literature [23, 24], studies dealing with their manufacturing and utilization are relatively scarce. Therefore, we have decided to study the microstructure, melting behavior and oxidation stability of Ce–Sn pre-alloy used for lead-free solder alloy manufacturing.

Experimental

Ce2Sn98 (composition in mass%) pre-alloy was prepared by melting of pure Sn (99.99 mass%) and Ce (99.9 mass%) in Al_2O_3 crucible in induction furnace. The furnace chamber was evacuated and purged three times with

✉ Marian Drienovsky
marian.drienovsky@stuba.sk

[1] Faculty of Materials Science and Technology in Trnava, Slovak University of Technology in Bratislava, Paulinska 16, 917 24 Trnava, Slovakia

protective Ar (99.9999 vol%) before melting. To homogenize the alloy, a mechanical stirring with quartz-glass rod was employed during melting. The molten alloy was rapidly solidified on a stainless steel plate, and cast strips have been formed. The stripes were cut into rectangular specimen, and samples with appropriate dimensions were taken for next experiments.

The preparation of metallographic sample consisted of cold pre-alloy mounting in resin, grinding on abrasive papers and polishing by Buehler diamond suspensions (in order 9, 6, 3 and 1 μm, respectively). The alloy polishing was terminated with an extra-fine alumina suspension. Light microscopy (Neophot 30), scanning electron microscopy (SEM, JEOL JSM7600F), energy-dispersive X-ray spectroscopy (EDX) and X-ray diffraction (XRD, Philips PW 1830 X-ray diffractometer with Bragg–Brentano geometry) were used to characterize the alloy microstructure and identify the phases present in the alloy.

The alloy melting behavior and oxidation stability were studied by differential thermal analysis coupled with thermogravimetry (DTA–TG) and differential scanning calorimetry (DSC). A simultaneous thermal apparatus Netzsch STA409CD was employed during both measurements. The scanning rate was 10 °C min^{-1} for both heating and cooling regimes. The experiments were conducted in a synthetic air (mixture of N_2 and O_2 with purity of 99.999 vol% in 80/20 vol% ratio) and inert gas (Ar, 99.9999 vol%) atmospheres. The same procedure of DTA–TG analysis was employed also for tin sample (Sn 99.99 mass%) which served as reference material for thermal analysis.

Additional experiments with two Ce2Sn98 samples were done. First, the samples were placed in two tiny alumina crucibles, heated in air in an external furnace and subsequently cooled. A temperature program similar to DTA–TG experiment was used. The mass of each sample was approximately 1 g. After heat treatment, the oxidation products from one sample were carefully scratched and taken for XRD measurement. The second sample was carefully vertically sectioned and cold-mounted in a conductive resin for subsequent SEM–EDX analysis.

Results and discussion

Initial microstructure and thermal analysis

The Ce2Sn98 pre-alloy was found to be composed of two different microstructure constituents. The detail of the alloy microstructure is provided in Fig. 1. Metal concentrations of the constituents are given in Table 1. The matrix of the alloy was composed of tin (Table 1). It is found in literature that tin forms a solid solution with cerium [23]. Nevertheless, due to relatively low elemental resolution of

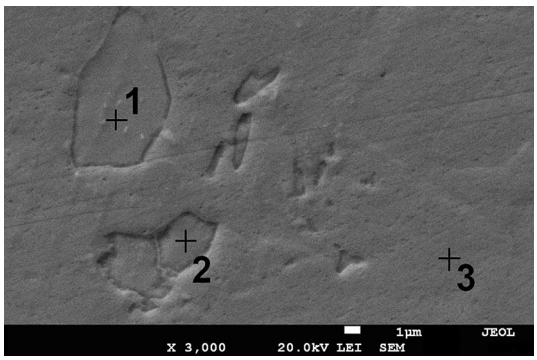

Fig. 1 Microstructure of alloy Ce2Sn98 documented by means of SEM. Metal concentrations corresponding to *points 1–3* are given in Table 1

Table 1 Metal concentrations of points 1–3 in Fig. 1 estimated with SEM/EDX

Point	Concentration/at.%		Constituent
	Sn	Ce	
1	74.55	25.45	$CeSn_3$
2	75.29	24.71	$CeSn_3$
3	100.00	–	Sn

EDX method, only Sn was identified. In the matrix, evenly distributed irregularly shaped particles with sizes of 1–10 μm have been found. Metal compositions of these particles were estimated from five point EDX measurements. The average metal composition was identified to be 74.7 at.% Sn and 25.3 at.% Ce (see metal concentrations of points 1 and 2 in Table 1). These metal concentrations correspond to $CeSn_3$. The room-temperature XRD pattern of Ce2Sn98 alloy is shown in Fig. 2. Sn as a major constituent and $CeSn_3$ as a minor constituent were identified.

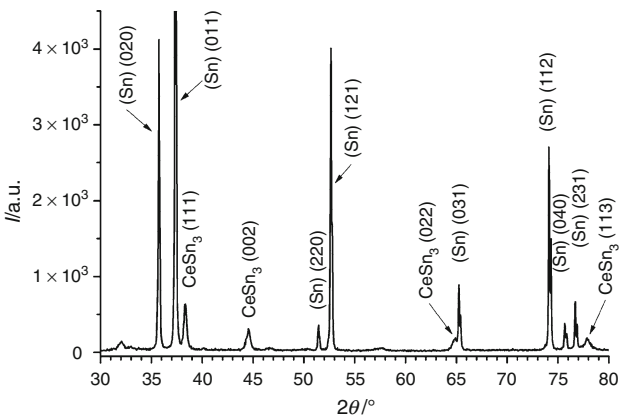

Fig. 2 Room-temperature XRD pattern of Ce2Sn98 alloy

Simultaneous DTA–TG and derivative thermogravimetry (DTG) curves of Ce2Sn98 and pure Sn are shown in Fig. 3a, b. For reader's convenience, the timescale on the x-axis was replaced by temperature scale. Two endothermic peaks at 243 and 500 °C and one exothermic peak at ~750 °C have been found on the DTA curve of the Ce2Sn98 alloy upon heating. The DTA of Sn sample (bottom curve in Fig. 3a) shows one narrow endothermic and two overlapping exothermic peaks located between 600 and 710 °C. The first endothermic peaks correspond to melting of the alloy and tin, respectively. The melting temperature of Sn found in this study is 233.1 °C, which is 1.2 °C higher than literature data [25]. This discrepancy is probably due to a fact that the DTA method is not as accurate as DSC. The first endothermic peak of the Ce2Sn98 alloy was found at lower temperature (232.6 °C), which suggests that Ce addition decreases the melting point of the alloy to the eutectic temperature. The second peak corresponds to liquidus temperature of the Ce2Sn98 alloy [23].

The TG–DTG curves are shown in Fig. 3b. It can be observed that mass of Ce2Sn98 and Sn samples starts to increase at 513 and 552 °C, respectively. The maximum mass gain of the Ce2Sn98 alloy is found at 767.8 °C during heating and at 920 °C during cooling in the case of Sn. The total mass gain of both samples is about 8 %. All the

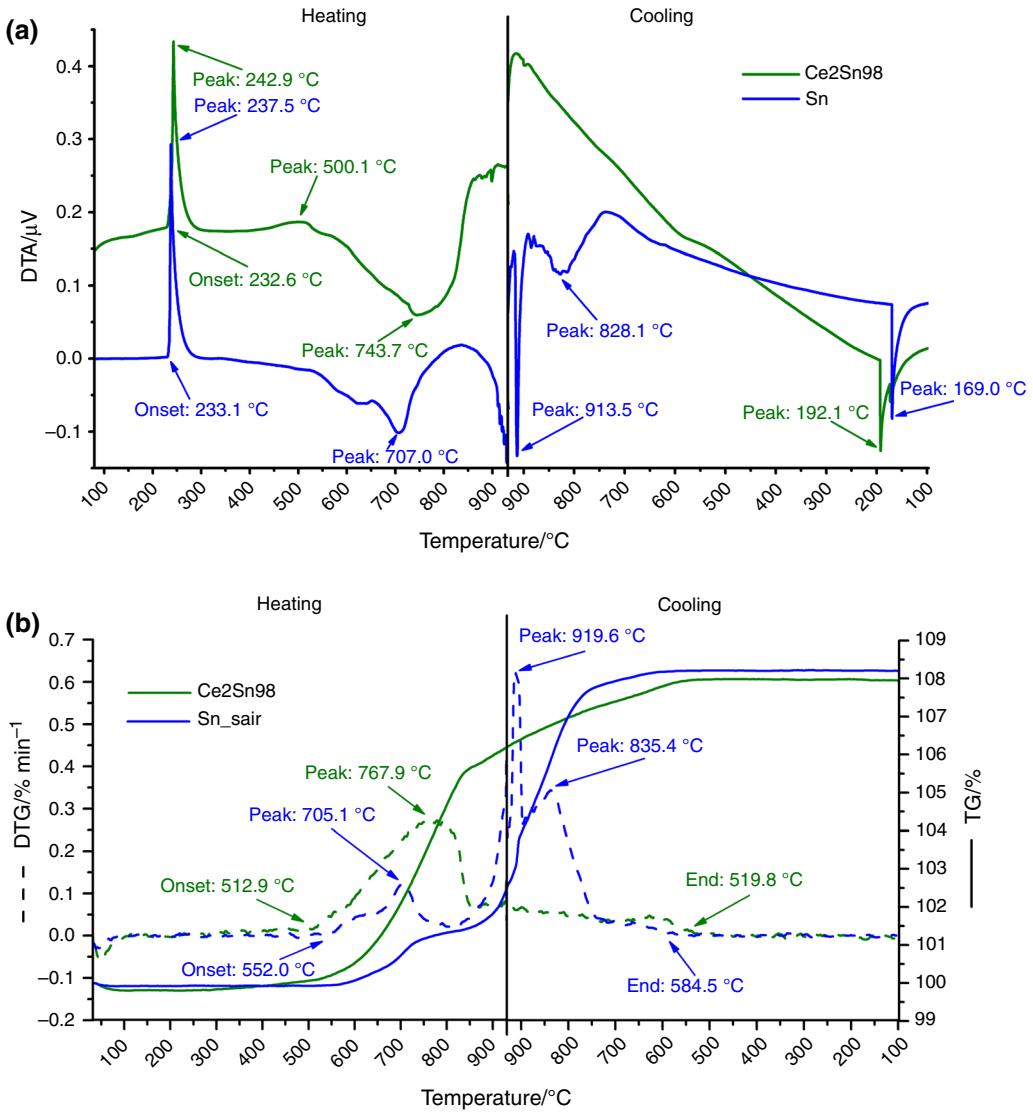

Fig. 3 Simultaneous DTA (**a**) and TG–DTG (**b**) measurement of Ce2Sn98 alloy (36.5 mg) and Sn (36.8 mg), heating 10 °C min^{-1}, air atmosphere

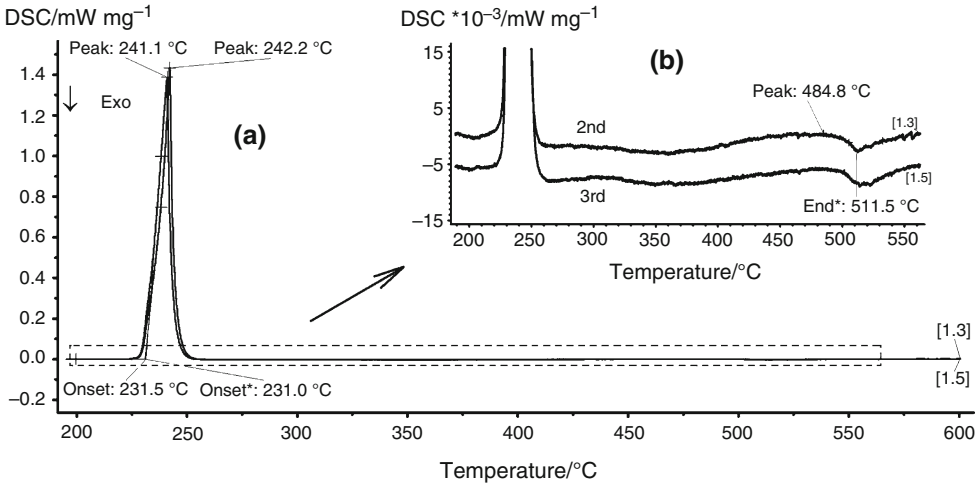

Fig. 4 DSC measurement of Ce2Sn98 alloy: an overview (**a**); detailed view of dashed rectangle (**b**) (25.7 mg, Al pans, second and third heating 10 °C min^{-1}, Ar 60 mL min^{-1})

exothermic peaks observed on the DTA curve in temperature range 500–930 °C are reversely proportional to DTG curve (dashed lines) suggesting a relation to the alloy oxidation at high temperatures. The last exothermic peaks at temperatures below 200 °C on the DTA curves represent a solidification of the samples. The exothermic effects at higher temperatures combined with the mass gain observed on the TG curves are related to an oxygen uptake from air. Chuang [26] provided a detailed study of the oxidation mechanism of $CeSn_3$ precipitates. According to the study, $CeSn_3$ reacts with ambient O_2 to form CeO_2 layer and tin whiskers. The CeO_2 layer is not homogeneous as it contains many sprouts of these long tin whiskers. This effect, however, concerns only grains on the surface. The observed rapid mass gain at temperatures higher than 500 °C (Fig. 3b) suggests that the volume oxidation of the Ce2Sn98 alloy started to take place immediately after reaching the liquidus temperature.

One possible explanation for this observation is that cerium metal is lighter than tin [25]. As such, it is able to float on the surface of the melt and speed up the oxidation process. Figure 3b shows that Ce in the Ce2Sn98 alloy oxidized more rapidly compared with Sn. The oxidation process of this alloy has been slowing down during cooling. On the other hand, Sn started to oxidize rapidly between 920 and 800 °C.

The DSC measurements of the Ce2Sn98 alloy were carried out in Ar gas. The results are presented in Fig. 4. Three heating steps and two cooling steps were done; however, second and third heating steps are shown. Both DSC curves were identical. In each DSC record, two peaks were identified: the first peak corresponds to melting of the Sn–Ce eutectic at 231 °C and the second peak is related to liquidus of the alloy determined as peak temperature at 485 °C [27]. The observed eutectic temperature and the peak temperature of liquidus of this system are in agreement with recently published phase diagram [23]. Since no further exothermic signals have been found, the Ce2Sn98 alloy has not been oxidized in argon. As such, the pre-alloy can be repeatedly melted in inert atmospheres during solder manufacturing.

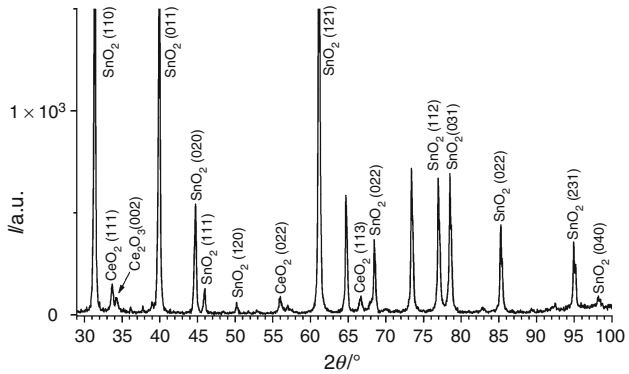

Fig. 5 XRD pattern of oxidized Ce2Sn98 alloy

Sample oxidation analysis

Two Ce2Sn98 samples were oxidized in air in an electrical furnace. A temperature program similar to previous DTA–TG experiment was applied. After oxidation, the surface oxides were carefully scratched from one sample and subjected to the XRD measurement. The XRD pattern is shown in Fig. 5. The presence of two oxides, SnO_2 and CeO_2, was confirmed. These oxides were found in different amounts, with SnO_2 being the major oxidation product. The XRD pattern also indicates the presence of small amounts of other oxidation products which, however, could not be precisely identified. These oxidation products are probably various cerium oxides since the Ce–O system contains many substoichiometric compositions [28].

The second sample was cross-sectioned and subjected to SEM/EDX microanalysis. The sample microstructure is presented in Figs. 6 and 7. The microstructural analysis of the inner sample areas revealed the presence of tin grains with regularly distributed small dark particles. By an overall EDX analysis, we could only find a minimal presence of Ce (approximately 0.1 mass%). On the metal surface, we found a heterogeneous and highly porous oxide layer with many cracks. Figures 6 and 7 show that this oxide layer is composed of two or more different oxides. For better clarification of the observed microstructure, three types of EDX measurements on the metal–oxide interface were conducted: point microanalysis (Fig. 6), elemental mapping for Ce (Fig. 6) and line scan microanalysis (Fig. 7).

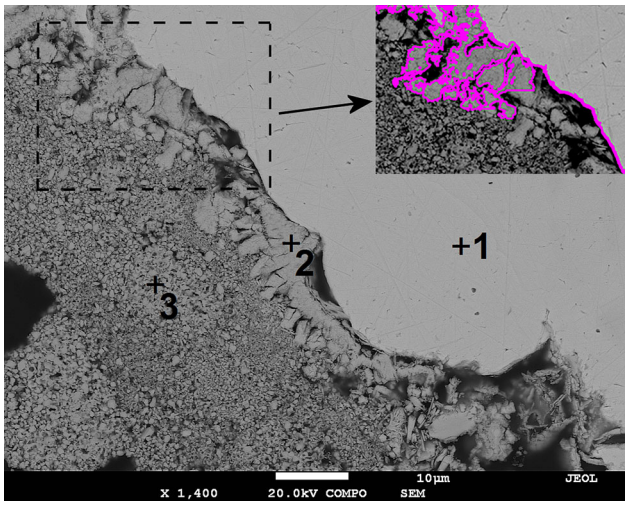

Fig. 6 Cross-sectional SEM micrograph of oxidized Ce2Sn98 alloy with EDX point microanalysis and mapping for Ce element (detailed part)

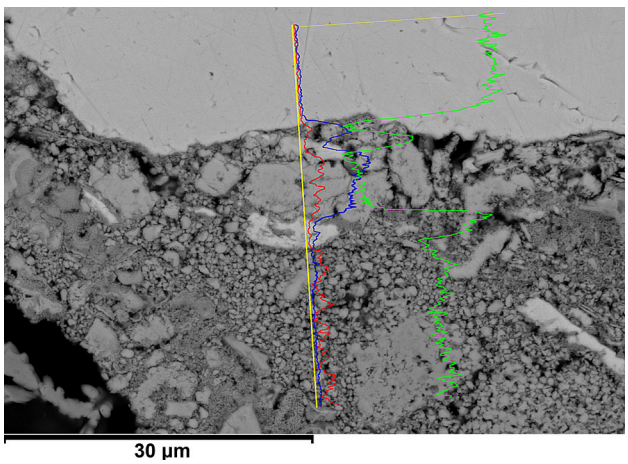

Fig. 7 SEM micrograph of oxidized Ce2Sn98 alloy with EDX line scan microanalysis (*green*—Sn; *blue*—Ce, *red*—O). (Color figure online)

In the case of the EDX point microanalysis, three points were chosen at three different places (see Fig. 6): an inner sample area (1), outer sample area (3) and interface between inner and outer areas (2). Results are given in Table 2. Point no. 1 analysis revealed the presence of tin only. No other elements have been found. Point no. 2 analysis revealed the presence of tin, cerium and oxygen with concentrations of 15.8, 19.2 and 64.9 at.%, respectively. Point no. 3 analysis showed only tin and oxygen with concentrations of 28.6 and 71.4 at.%, respectively. This composition is close to the SnO_2 stoichiometry.

The area between the bulk metal and the oxide scale was further analyzed by EDX element mapping and line scanning. The results are presented in Figs. 6 and 7. The inset in Fig. 6 shows the presence of Ce. This element was only found in the larger particles at the metal–oxide interface, as indicated by pink color. The EDX line scan is presented in Fig. 7. The green line represents Sn, blue line Ce and red line O. The SEM/EDX analysis showed that the bulk metal is composed of Sn mostly. The outer oxide scale is composed of Sn and O, suggesting a SnO_2 composition. At the interface between the outer oxide layer and inner bulk Sn, we detected a thin layer containing also Ce, next to Sn and O. This suggests that this layer is composed of either CeO_2 and SnO_2 or CeO_2 and Sn. Sn had been probably formed as a product of $CeSn_3$ particles decomposition during early stages of oxidation. This suggestion is further supported by EDX line scan shown in Fig. 7. We found two small sprouts, being composed of Sn mostly and being located next to a Ce-containing particle.

Practically, no presence of initial $CeSn_3$ particles in the inner microstructure suggests that after melting Ce oxides floated at the surface of liquid alloy during the oxidation experiment in the furnace. This has probably happened due to lower specific mass of Ce compared with Sn [25]. We believe that the explanation of the observed microstructure is as follows. $CeSn_3$ particles gradually melt between solidus and liquidus temperatures. Ce then aggregates at the surface of liquid alloy, and this segregation happens shortly after the alloy melting. At temperatures above 500 °C, Ce starts to oxidize rapidly, which is shown on the simultaneous DTA–TG–DTG analysis (Fig. 3a, b). The product of oxidation is both Ce_2O_3 and CeO_2. Since Ce_2O_3

Table 2 Elemental concentrations of points 1–3 in Fig. 6 measured by SEM/EDX

Point	Concentration/at.%		
	Sn	Ce	O
1	100.00	–	–
2	15.84	19.22	64.94
3	28.56	–	71.44

has a higher enthalpy of formation compared with CeO_2, it ultimately reacts with oxygen to form CeO_2 [17]. Due to the structural changes in Ce oxides, the cerium oxide film is not homogenous. As such, it has many cracks. The liquid tin, located under the oxide scale, is therefore partially exposed to oxygen from air. According to Yuan et al. [29], the outward diffusion of Sn atoms is more likely to take place than the inward diffusion of the oxidant (O_2). Sn initially forms SnO which is, however, not stable at higher temperatures and quickly decomposes to Sn and SnO_2 [29]. This process is repeated and further accelerated with increasing temperature. Finally, no free Sn is left on the surface. Furthermore, the additional oxide layer of CeO_2, which has been formed first, can partially obstruct the outward Sn diffusion from the melt which may ultimately slow down the oxidation of Sn at higher temperatures. This is clearly indicated on the TG–DTG curve, given in Fig. 3 b, where the measurement of Ce2Sn98 alloy is compared with pure Sn.

Conclusions

Ce2Sn98 (mass%) pre-alloy was prepared by controlled melting of pure Sn and Ce in high purity Ar (99.9999 vol.%). The master alloy was rapidly solidified in the form of cast strips. The alloys microstructure was composed of randomly distributed $CeSn_3$ particles in the Sn matrix.

The melting of this alloy was observed to start at 231 °C and to finish at liquidus temperature of 485 °C, respectively. Simultaneous DTA–TG–DTG thermal analysis revealed that both samples (Sn and Ce2Sn98) started to oxidize at temperatures higher than 500 °C. However, in the case of latter sample a rapid alloy oxidation was taking place after melting in air. Due to high reactivity of $CeSn_3$ with oxygen, the Ce–Sn master alloy has to be re-melted in an inert atmosphere during additional processing, as shown by the DSC measurement in argon.

The XRD and SEM/EDX experiments on the Ce2Sn98 samples after oxidation have been done to clarify the oxidation process. It was found that Ce atoms emerge from the liquid alloy during melting. These atoms react with oxygen as first and form a heterogeneous cerium oxide scale on the sample surface. Sn is oxidized afterward. Due to the outward diffusion of Sn through the heterogeneous Ce oxide layer, the SnO is formed. Since this oxide is not stable at higher temperatures, it decomposes to SnO_2 and Sn. This process is repeated until no free Sn is left on the surface.

Acknowledgements This work is the result of the project implementation: Centre of excellence for development and application of advanced diagnostic methods in processing of metallic and non-metallic materials, ITMS:26220120048, supported by the Research and Development Operational Programme funded by the European regional development fund. The authors would also like to acknowledge the Project No. 1/0068/14 funded by the Grant Agency VEGA.

References

1. Wang W-T, Zhang X-M, Gao Z-G, Jia Y-Z, Ye L-Y, Zheng D-W, Liu L. Influences of Ce addition on the microstructures and mechanical properties of 2519A aluminum alloy plate. J Alloys Compd. 2010;491:366–71.
2. Wu L, Cui Ch, Wu R, Li J, Zhan H, Zhang M. Effects of Ce-rich RE additions and heat treatment on the microstructure and tensile properties of Mg–Li–Al–Zn-based alloy. Mater Sci Eng A. 2011;528:2174–9.
3. Jeong HY, Kim B, Kim S-G, Kim HJ, Park SS. Effect of Ce addition on the microstructure and tensile properties of extruded Mg–Zn–Zr alloys. Mater Sci Eng A. 2014;612:217–22.
4. Zhang Q, Tong L, Cheng L, Jiang Z, Meng J, Zhang H. Effect of Ce/La microalloying on microstructural evolution of Mg–Zn–Ca alloy during solution treatment. J Rare Earth. 2015;33(1):70.
5. Krupinski M, Krupinska B, Rdzawski Z, Labisz K, Tanski T. Additives and thermal treatment influence on microstructure of nonferrous alloys. J Therm Anal Calorim. 2015;120:1573–83.
6. Loomans ME, Fine ME. Tin–silver–copper eutectic temperature and composition. Metall Mater Trans A. 2000;31A:1155–62.
7. Moon KW, Boettinger WJ, Kattner UR, Biancaniello FS, Handwerker CA. Experimental and thermodynamic assessment of Sn–Ag–Cu solder alloys. J Electron Mater. 2000;29:1122–236.
8. Pilloni M, Ennas G, Cabras V, Denotti V, Kumar VB, Musinu A, Porat Z, Scano A, Gedanken A. Thermal and structural characterization of ultrasonicated Bi–Sn alloy in the eutectic composition. J Therm Anal Calorim. 2015;120:1543–51.
9. Kim KS, Huh SH, Suganuma K. Effects of cooling speed on microstructure and tensile properties of Sn–Ag–Cu alloys. Mater Sci Eng A. 2002;333:106–14.
10. Palcut M, Sopousek J, Trnkova L, Hodulova E, Szewczykova B, Ozvold M, Turna M, Janovec J. Thermal analysis of selected tin-based lead-free solder alloys. Kovove Mater. 2009;47:43–50.
11. Mookam N, Kanlayasiri K. Effect of soldering condition on formation of intermetallic phases developed between Sn–0.3Ag–0.7Cu low-silver lead-free solder and Cu substrate. J Alloys Compd. 2011;509:6276–9.
12. Fima P, Gazda A. Thermal analysis of selected Sn–Ag–Cu alloys. J Therm Anal Calorim. 2013;112:731–7.
13. Chriastelova J, Trnkova LR, Dimova KP, Ozvold M. Reaction of liquid Sn–Ag–Cu–Ce solders with solid copper. J Electron Mater. 2011;40:1956–61.
14. Drienovsky M, Trnkova LR, Martinkovic M, Ozvold M, Cernickova I, Palcut M, Janovec J. Influence of cerium addition on microstructure and properties of Sn–Cu–(Ag) solder alloys. Mater Sci Eng A. 2015;623:83–91.
15. Lee H-T, Chen Y-F, Schwedt A, Mayer J. Effect of La addition on adhesive strength and fracture behavior of Sn–3.5Ag solder joints. Mater Sci Eng. 2011;A528:3630–8.
16. Zeng G, Xue S, Gao L, Zhang L, Hu Y, Lai Z. Interfacial microstructure and properties of Sn–0.7Cu–0.05 Ni/Cu solder joint with rare earth Nd addition. J Alloys Compd. 2011;509:7152–61.
17. Konings RJM, Benes O, Kovacs A, Manara D, Sedmidubsky D, Gorokhov L, Iorish VS, Yungman V, Shenyavskaya E, Osina E. The thermodynamic properties of the f-elements and their compounds. Part 2. The lanthanide and actinide oxides. J Phys Chem Ref Data. 2014;43(2014):11–3.

18. Wang J-X, Xue S-B, Han Z-J, Yu S-L, Chen Y, Shi Y-P, Wang H. Effects of rare earth Ce on microstructures, solderability of Sn–Ag–Cu and Sn–Cu–Ni solders as well as mechanical properties of soldered joints. J Alloys Compd. 2009;467:219–26.
19. Zhang L, Xue S-B, Gao L-L, Sheng Z, Yu S-L, Chen Y, Dai W, Ji F, Guang Z. Reliability study of Sn–Ag–Cu–Ce soldered joints in quad flat packages. Microelectron Reliab. 2010;50:2071–7.
20. Zhang L, Xue S-B, Gao L-L, Dai W, Ji F, Chen Y, Yu S-L. Microstructure characterization of SnAgCu solder bearing Ce for electronic packaging. Microelectron Eng. 2011;88:2848–51.
21. Lin H-J, Chuang T-H. Effects of Ce and Zn additions on the microstructure and mechanical properties of Sn–3Ag–0.5Cu solder joints. J Alloys Compd. 2010;500:167–74.
22. Zhang L, Xue SB, Zeng G, Gao LL, Ye H. Interface reaction between SnAgCu/SnAgCuCe solders and Cu substrate subjected to thermal cycling and isothermal aging. J Alloys Compd. 2012;510:38–45.
23. Li J, Tao X, Dong S, Yang F, Liu H, Jin Z, Zheng F. Thermodynamic assessment of Sn–Cu–Ce system. CALPHAD. 2013;43:124–32.
24. Dong HQ, Tao XM, Laurila T, Vuorinen V, Paulasto-Krockel M. Thermodynamic modeling of Au–Ce–Sn ternary system. CALPHAD. 2013;42:38–50.
25. http://periodictable.com/Elements/050/data.html. Accessed 5 Feb 2016.
26. Chuang T-H. Rapid whisker growth on the surface of Sn–3Ag–0.5Cu–1.0Ce solder joints. Scr Mater. 2006;55:983–6.
27. Rycerz L. Practical remarks concerning phase diagrams determination on the basis of differential scanning calorimetry measurements. J Therm Anal Calorim. 2013;113:231–8.
28. Zinkevich M, Djurovic D, Aldinger F. Thermodynamic modelling of the cerium–oxygen system. Solid State Ion. 2006;177:989–1001.
29. Yuan D-W, Yan R-F, Simkovich G. Rapid oxidation of liquid tin and its alloys at 600–800°C. J Mater Sci. 1999;34:2911–20.